The University Of Sheffield.

This is a repository copy of *Thermodynamic interpolation for the simulation of two-phase flow of non-ideal mixtures*.

White Rose Research Online URL for this paper:
http://eprints.whiterose.ac.uk/108114/

Version: Accepted Version

White Rose
university consortium
Universities of Leeds, Sheffield & York

eprints@whiterose.ac.uk
https://eprints.whiterose.ac.uk/

Thermodynamic interpolation for the simulation of two-phase flow of complex mixtures

S. Brown[1,2], L. D. Peristeras[3], S. Martynov[2], R. T. J. Porter[2], H. Mahgerefteh[2,*], Ilias K. Nikolaidis[3], Georgios C. Boulougouris[3,4], Dimitrios M. Tsangaris[3] and Ioannis G. Economou[3,5]

*corresponding author h.mahgerefteh@ucl.ac.uk

[1]*Current address: Department of Chemical and Biological Engineering, The University of Sheffield, Mappin Street S1 3JD, UK*

[2]*Department of Chemical Engineering, University College of London, London WC1E7JE, UK*

[3]*National Center for Scientific Research "Demokritos", Institute of Nanoscience and Nanotechnology, Molecular Thermodynamics and Modelling of Materials Laboratory, Agia Paraskevi, Attikis GR–153 10, Greece*

[4]*Department of Molecular Biology and Genetics, Democritus University, 68100, Alexandroupolis, Greece*

[5]*Texas A&M University at Qatar, Chemical Engineering Program, 23874 Doha, Qatar*

Abstract

This paper describes the development and application of a technique for the rapid interpolation of thermodynamic properties of mixtures for the purposes of simulating two-phase flow. The technique is based on adaptive inverse interpolation and can be applied to any Equation of State and multicomponent mixture. Following analysis of its accuracy, the method is coupled with a two-phase flow model, based on the homogeneous equilibrium mixture assumption, and applied to the simulation of flows of carbon dioxide (CO_2) rich mixtures. This coupled flow model is used to simulate the experimental decompression of binary and quinternary mixtures. It is found that the predictions are in good agreement with the experimental data and that the interpolation approach provides a flexible, robust means of obtaining thermodynamic properties for use in flow models.

Keywords: Carbon dioxide transport, Two-phase flow, Equations of state, Pipeline safety

1. Introduction

The modelling of compressible two-phase or flashing flows is common place in a wide range of areas in engineering. For example, cavitation in automotive fuel injection systems (Martynov et al., 2006), flash boiling of water during loss-of-coolant accidents in nuclear reactors (Blinkov et al., 1993) and liquid boiling and expansion in refrigeration systems and heat pumps (Simões-Moreira and Bullard, 2003). Whilst various approaches are available to model the dynamics of two-phase flow, the accuracy of simulations for flashing two-phase flows to a large extent depends on the accuracy of

37   the physical properties data in use. This particularly applies to multi-component mixtures, which are
38   commonly found as working fluids in the above systems.

39   In practice, complex mathematical formulas known as Equations of State (EoS), are used to provide
40   the thermodynamic properties for both vapour and liquid phases. As a result, a practical problem
41   arises when pressure explicit EoS are coupled with flow models. In these EoS, the thermodynamic
42   properties are predicted as a function of pressure, temperature and composition while phase
43   equilibria, at a given system pressure and temperature (P-T), is determined using a variety of
44   isothermal 'flash' algorithms (M. Michelsen, 1982; M. L. Michelsen, 1982). This formulation contrasts
45   with the fluid-dynamics models, where the conservation laws governing are naturally posed in terms
46   of density and internal energy (ρ-U). To overcome this problem, one possible solution is to use the
47   so-called isochoric-isoenergetic flash (Castier, 2009; Michelsen, 1999). However, existing isochoric-
48   isoenergetic flash algorithms are neither robust nor computationally efficient in the context of flow
49   simulation because they either rely on an internal iterative loop over the P-T variables (Michelsen,
50   1999; Saha and Carroll, 1997) or on the direct minimisation of total entropy (Castier, 2009;
51   Munkejord and Hammer, 2015).

52   The problem of computational inefficiency is exacerbated by the complexity of modern EoS. For
53   example, for the case of CO_2 and its mixtures, high accuracy is provided by SAFT EoS (Diamantonis
54   and Economou, 2011) or by the "reference" EoS (Span and Wagner, 1996) and both EoS have a large
55   number of relatively complex terms. As a result, application of these EoS to flow simulations not only
56   increases the computational cost, but also the susceptibility to numerical instabilities in the
57   underlying isothermal flash algorithms.

58   This is a particular problem in the simulation of flows associated with Carbon Capture and Storage
59   (CCS), where the CO_2 stream may contain a number of impurities and vary in composition (Porter et
60   al., 2015). Indeed, it is well established that the presence of these impurities has important impacts
61   on many aspects where the modelling of two-phase flow is relevant, including ductile fracture
62   (Mahgerefteh et al., 2012a) and the release rate in the case of loss of containment (Brown et al.,
63   2013).

64   Previous work to address this issue has focused on producing tables of thermodynamic properties
65   from isenthalpic or isentropic flash calculations (Mahgerefteh et al., 2006), which are facilitated by
66   changing the variables with which the flow is resolved, or using isothermal tables for use in the
67   iterative loop (Andresen, 2009). The former of these means that alternative numerical techniques
68   must be applied and that conservation of mass, momentum and energy is not ensured. Dumbser et
69   al. (2013) presented a method of building an interpolating function using adaptive mesh refinement
70   for a single component fluid; however this relied on the ability to calculate isochoric-isoenergetic
71   flashes which cannot be done efficiently for mixtures.

72   In this work a robust technique for efficiently performing isochoric-isoenergetic flashes, for the
73   purposes of two-phase flow calculations, is presented. The technique is based on adaptive inverse
74   interpolation and can be applied independently of the EoS and the specific mixture under
75   consideration. The technique is intended for the application of the complex, computationally heavy
76   EoS that are required for the accurate prediction of the thermodynamic properties and phase
77   equilibria of CO_2 mixtures. This is then coupled with a two-phase flow model based on the
78   homogeneous equilibrium mixture assumption (Brown et al., 2015a; Mahgerefteh et al., 2012b) and
79   applied to the simulation of CCS relevant two-phase flows.

80 This paper is structured as follows: Section 2 firstly presents the fluid flow model applied in this
81 study (Section 2.1) followed by a description of the interpolation technique developed (Section 2.2).
82 The section ends with an overview of the EoS used in this work.

83 Section 3 provides an analysis of the interpolation technique's consistency with the EoS (Section
84 3.1). Next, the method is coupled with the two-phase flow model and a number of tests are
85 performed to establish the robustness and computational efficiency of the method in the presence
86 of rapid transients (Section 3.2). This coupled flow model is then used to predict the decompression
87 of several mixtures and the results are compared against available experimental data (Section 3.3).
88 Conclusions and suggestions for future work are discussed in Section 4.

2. Methodology

2.1. The Homogeneous Equilibrium Model (HEM) flow model

91 The model applied in this study is based on the assumptions of one-dimensional, unsteady flow and,
92 in the case of two-phase flow, thermodynamic and mechanical equilibrium, i.e. a single temperature,
93 pressure and velocity, between the saturated vapour and liquid phases. In this case the respective
94 continuity, momentum, and energy conservation equations are given by (see for example Zucrow
95 and Hoffman, 1975):

$$\frac{\partial \rho}{\partial t} + \frac{\partial \rho u}{\partial z} = 0 \tag{1}$$

96

$$\frac{\partial \rho u}{\partial t} + \frac{\partial \rho u^2 + P}{\partial z} = -\frac{f_w \rho u^2}{D_p} \tag{2}$$

97

$$\frac{\partial E}{\partial t} + \frac{\partial u(E + P)}{\partial z} = -u\frac{f_w \rho u^2}{D_p}. \tag{3}$$

98 where ρ, u, P are respectively the mixture density, velocity and pressure, which are functions of
99 time, t, and spatial coordinate, z; D_p and f_w, are the pipeline diameter and Fanning friction factor,
100 calculated using Chen's correlation (Chen, 1979), and E is the total mixture energy defined as:

$$E = \rho \left(e + \frac{1}{2}u^2 \right) \tag{4}$$

101 where e is the mixture specific internal energy:

$$e = x_{eq}e_v + (1 - x_{eq})e_l \tag{5}$$

102 x_{eq} is the equilibrium vapour quality, and ρ is the mixture density defined as:

103

$$\frac{1}{\rho} = \frac{x_{eq}}{\rho_v} + \frac{(1 - x_{eq})}{\rho_l}. \tag{6}$$

104 In equations (5) and (6) the subscripts v and l refer to the vapour and liquid phases respectively.

105   To solve equations (1) to (3) numerically, a finite volume method is used (Leveque, 2002), where,
106   following Brown et al. (2015b), the conservative left-hand-side of equations (1) to (3) are solved
107   using the AUSM-+ flux vector splitting scheme (Liou, 2006).

108 2.2.Interpolation technique

109   As described previously, the coupling of the EoS described in Section 2.3 with the flow equations ((1)
110   to (3)) where the fluid is two-phase is complicated by the fact that the free variables are the density,
111   ρ, and internal energy, e, with which we must compute the system P and T, while the computation
112   of the phase equilibria using an EoS (in this case PC-SAFT as described in section 2.3) is most
113   commonly performed using the P and T of a mixture at a given composition. To overcome this, we
114   introduce the construction of two interpolant grids, one of which is constructed using the P and T as
115   free variables, denoted {P, T}, and the other using ρ and e, denoted by {ρ,e}. These grids provide the
116   means for rapidly computing the thermodynamic properties and phase equilibria during flow
117   simulations.

118   The construction begins by defining the bounds of the {P,T} grid using the fluid conditions required
119   for the simulation (i.e. the intervals [T_{min}, T_{max}] and [P_{min}, P_{max}]). Grid points are sampled along
120   isotherms which are uniformly distributed within the temperature range. Typically, for the pressure
121   ranges of interest for CO_2 pipeline decompression, the isotherms will intersect the dew and bubble
122   point and hence pass through the phase envelope. As a result, an interpolant has to be developed
123   which can resolve the abrupt changes of the fluid properties with pressure and temperature within
124   the phase coexistence regions, and in particular near the equilibrium lines. In practice this means
125   that the points selected for building the interpolant cannot be uniformly distributed along the
126   isotherm, but must be chosen so as to resolve the region around, and within, the phase envelope of
127   the mixture, which is known *a priori* given the composition of the fluid.

128   In order to address this problem and improve the mapping, we adopt a non-uniform sampling along
129   each isotherm, resulting in an increased density of points close to the dew and bubble point
130   pressures (P_d and P_b respectively) and within the phase envelop itself. The set of N points along
131   each isotherm are selected as follows:

132   a. if $P_{max} \leq P_d$ or $P_b \leq P_{min}$, i.e. a permanently single-phase fluid, the points are
133   uniformly distributed in [P_{max}, P_{min}]:

$$P_i = P_{min} + (i-1)\frac{P_{max} - P_{min}}{N-1}, \quad i = 1, \ldots, N \tag{7}$$

132   b. if $P_{min} \leq P_d \leq P_b \leq P_{max}$, i.e. the interval [$P_{min}, P_{max}$] encompasses the two-phase
135   region, N_d points are distributed in [$P_{min}, P_d - \Delta$] to increase the point density close
136   to the dew point using:

$$P_i = P_{min} + (P_d - \Delta - P_{min})\, g\left(\frac{i-1}{N_d}\right), \quad i = 1, \ldots, N_d \tag{8}$$

137   N_b points are distributed uniform in [$P_b + \Delta, P_{max}$] to increase the point density
138   close to the bubble point using:

$$P_i = (P_b + \Delta - P_{min}) + (P_{max} - P_b - \Delta)\, g\left(\frac{i-1}{N_b}\right), \quad i = 1, \ldots, N_b \tag{9}$$

139   while the remaining N_{VLE} points are distributed using the mapping function which
140   increases the points density near the dew and the bubble line:

$$P_i = (P_d - \Delta) + (P_b - P_d + 2\Delta)\, g\left(\frac{i-1}{N_{VLE}}\right), \quad i = 1, \ldots, N_{VLE} \tag{10}$$

141   with:

$$g(x) = \frac{1 + erf(Ax - B)}{2} \tag{11}$$

142   c.   if $P_{min} \leq P_d \leq P_{max} \leq P_b$ or $P_d \leq P_{min} \leq P_b \leq P_{max}$, i.e. the interval $[P_{min}, P_{max}]$ contains
143   part of the two-phase region a variant of the points distribution described in case b
144   is applied. For example if $P_{min} \leq P_d \leq P_{max} \leq P_b$, the points are distributed according to
145   (8) and (10), with the exception that in (10) P_{max} is taken as the upper limit rather
146   than $P_b + \Delta$.

147   In case b, the most general, the number of points N_{VLE} is taken as 70 % of the total number N, while
148   N_d and N_b are each taken as 15 % of N. The total number of points, N, as well as the distribution
149   function parameters Δ, A and B are tuned to optimise grid's quality. In this study A and B were set
150   equal to 4.4 and 2.2 respectively while the values used for N and Δ are reported in later sections.

151   At each of these points, using the P and T, the other thermodynamic properties are calculated (e.g. e,
152   ρ). In other words, at these points we have established the maps $e(P,T)$ and $\rho(P,T)$. Using these same
153   points we re-interpret the grid to give us the inverse maps P(e, ρ) and T(e, ρ), and hence a $\{\rho, e\}$ grid.

154   In order to increase the accuracy of this new grid across the ranges of densities and internal energies
155   covered, we redistribute the points along an isotherm map T(e, ρ) crossing the phase envelope. The
156   corresponding path is expressed as a mono-parametric curve ($e(\lambda)$, $\rho(\lambda)$) with $0.0 \leq \lambda \leq 1.0$.
157   Eventually, the properties of interest along this curve are also expressed as functions of the same
158   parameter i.e. T(λ), P(λ). Using appropriate values of λ we resample the path to obtain more
159   uniformly distributed points along the isotherm while the desired properties at the new point are
160   calculated by interpolating the corresponding functions using univariate Akima splines (Akima,
161   1996). Finally, we resample the $\{\rho, e\}$ grid produced for each property of interest by using the
162   bivariate Akima spline interpolation scheme (Akima, 1996) to improve its uniformity/regularity and
163   consequently the efficiency of the interpolation.

164   ## 2.3. Equations of State

165   In the present study in order to predict the properties of CO_2 and its mixtures, the Perturbed Chain-
166   Statistical Associating Fluid Theory (PC-SAFT) EoS presented by Diamantonis et al. (2013a) is applied,
167   a brief description is given next. The PC-SAFT EoS is expressed as the summation of residual
168   Helmholtz free energy terms that occur due to different types of intermolecular interactions
169   between the various components in the system under study. The residual Helmholtz free energy,
170   A_{res} is equal to the Helmholtz free energy minus the Helmholtz free energy of the ideal gas at given
171   temperature and density. For a system that consists of associating chains (for example aqueous
172   mixtures), PC-SAFT can be expressed as:

$$\frac{A^{res}(\rho, T)}{NRT} = \frac{a^{hs}}{RT} + \frac{a^{chain}}{RT} + \frac{a^{disp}}{RT} + \frac{a^{assoc}}{RT}, \tag{12}$$

173 where a is the Helmholtz free energy per mole, R is the universal gas constant and the superscripts
174 "res", "hs", "chain", "disp", and "assoc" refer to residual, hard sphere, chain (hard chain reference
175 fluid), dispersion, and association, respectively. The mathematical expressions for the individual
176 terms may be found in Diamantonis et al. (2013b). More details on the SAFT EoS and its variants for
177 pure components and their mixtures are given in Kontogeorgis and Folas (2010).

3. Results and discussion

178

3.1. Interpolation consistency analysis

179

180 Prior to its application to flow simulations the consistency of the interpolation method with the
181 underlying thermodynamic model must be assessed. For the subsequent analysis, two mixtures are
182 chosen; a simple binary mixture of CO_2 and nitrogen (N_2) and a more complex quinternary mixture of
183 hydrogen (H_2), oxygen (O_2), N_2, methane (CH_4) and CO_2 (Tests 26 and 31 respectively presented by
184 Cosham et al., 2012). The composition of each mixture is shown in Table 1. The construction of the
185 tables used a total of 100 isotherms along which N was taken to be 200, while Δ is set to zero. It
186 should be noted that, due to the extended P and T conditions of the experimental data, and hence
187 lower pressures and temperatures, produced for the binary mixture presented in Section 3.3, it is
188 necessary to produce a table which extends to far lower temperatures. Figures 1 (a) and (b)
189 respectively show the points sampled for the $\{\rho, e\}$ constructed for the binary mixture using a
190 uniform $\{P,T\}$ grid and using the methodology developed above. The $\{P,T\}$ grid developed for this
191 latter is shown in Figure 2. As can clearly be seen in Figure 1 (a) the "uniform sampling strategy"
192 produces in a much sparser weighting of the points through the phase envelope compared to the
193 one achieved in (b) where the re-distribution of the points results in a much greater number of
194 samples between the dew and bubble point lines.

195 In order to quantify the deviations of the predictions obtained from the interpolation grids and the
196 actual values calculated from the underlying EoS, 10,000 random samples are taken in the relevant
197 P-T domain. From these samples, the $e(P,T)$ and $\rho(P,T)$ functions are evaluated using the EoS and the
198 application of the interpolation grids using these values compared with the original point. Table 2
199 presents the percentage average absolute deviations (% AAD) of the predictions obtained from this
200 analysis for both the binary and quinternary mixtures. It should be noted that the grid produced
201 from the uniform $\{P,T\}$ sampling failed to provide predictions for all of the points used in this
202 comparison and so is omitted. As may be observed, with the exception of the binary pressure
203 predictions for which a value of 0.44 % was found, the results show an AAD% of less than 0.1%.

204 Figures 3 (a) and (b) show the %AAD contours of the predicted temperature and pressure
205 respectively, for the binary mixture. Figures 4 (a) and (b) shows the same data for the quinternary
206 mixture. As can be seen from both Figures 3 and 4 the error observed in the prediction of the
207 pressure is substantially higher in places, reaching up to 10 %, than for the temperature, which is
208 less than 0.5 % throughout; nevertheless, the regions of high error are restricted to low
209 temperatures above the bubble point line which has limited physical interest. It should further be
210 noted that this region also corresponds to conditions where solid formation may be expected, which
211 however is not accounted for in the current thermophysical model.

3.2. Shock tube tests

212

213 In order to assess the efficacy of the interpolation technique developed in this work as a means of
214 providing thermodynamic properties to flow simulations, two shock tube tests conducted are

215 simulated. For the first simulation, the states are chosen such that the fluid remains in the single-
216 phase region. For the second simulation the states are chosen to induce phase change in an initially
217 single-phase state. The conditions for the single and two-phase shock tube tests can be found in
218 Tables 3 and 4 respectively. In both cases, simulations are performed for both the binary and
219 quinternary mixtures using a CFL number of 0.2 and 200 computational cells.

3.2.1. Single phase

221 Figures 5 (a) to (c) show the profiles of the density, pressure and temperature respectively for both
222 the binary and quinternary mixture. As may be observed from Figure 5 (a) for the density of the
223 binary mixture, an expansion wave is observed at ca. 0.3 to 0.4 separating two constant states; this
224 is followed by a jump in the density across the discontinuity at ca. 0.6 before a smooth drop
225 beginning at ca 0.8 and ending at ca. 0.9. It is clear that the features of the results for the
226 quinternary mixture are the same as in the binary case, with the exception that they are at a lower
227 density level.

228 For the pressure (Figures 5 (b)) the results for both the binary and quinternary mixtures are almost
229 identical; as expected the discontinuity is still present. The slight variations are likely due to the
230 slight differences in the speed of sound and hence wave speeds. The temperature results show the
231 same similarities between the two mixtures (Figure 5 (c)). Importantly, the interpolated results
232 remain stable despite the presence of shock and rarefaction waves as well as contact discontinuities.

3.2.2. Two-phase

234 Figure 6 (a) to (d) shows the profiles of the density, vapour fraction, pressure and temperature
235 respectively, for the binary and quinternary mixtures. While the left hand states are the same and
236 the fluid is in the single-phase region, the state on the right is selected within the mixture's phase
237 envelope. Thus, relative to the dew line, the states are different for both of the two mixtures
238 simulated.

239 As Figure 6 (a) shows, for the binary mixture the density falls across the expansion wave which
240 begins at ca. 0.3 m and ends at ca. 0.4 m. The density drops sharply at 0.58 m, where the initial
241 boundary between the states was placed; this is followed by a slight distortion of the discontinuity at
242 ca. 0.62 m, representing an additional wave, and a slower drop across the shock between 0.64 m
243 and 0.68 m. Similar trends are observed for the quinternary mixture. However, the density
244 throughout is lower and the shock wave from 0.64 m is smeared over a larger distance.

245 The profiles of the vapour fraction (Figure 6 (b)) show that no vapour is produced across the
246 expansion wave. The vapour fraction is seen to increase through the series of waves between 0.58 m
247 and 0.64 m. Interestingly, across the shock wave, the vapour fraction increases for the binary and
248 decreases for the quinternary mixture, which is due to the different phase equilibria through the
249 respective mixture's phase envelopes.

250 Following the expansion wave, the pressures (Figure 6 (c)) obtained prior to the shockwaves is
251 substantially higher for the quinternary mixture, and in both cases relates to the bubble line
252 pressure of the fluids. In the case of the temperature (Figure 6 (d)), a fall is observed through the
253 expansion wave as with the density, after this however a sharp fall is seen at discontinuity before
254 rising and falling again. For this latter behaviour the quinternary mixture exhibits much larger
255 changes.

256 ## 3.3. Decompression tests

257 In the following, the robustness of the HEM outflow model coupled with the interpolation technique
258 is evaluated for pipeline releases of CO_2 mixtures. The outflow model is validated against two sets of
259 experimental data obtained from Full-Bore Rupture (FBR) releases of CO_2 from a 144 m long, 150
260 mm internal diameter section of pipeline using the two mixtures introduced earlier (Cosham et al.,
261 2012). Table 1 presents the initial conditions and composition of fluid in the pipeline in both cases.
262 Given the very short depressurisation durations considered in both tests, heat transfer between the
263 pipe wall and the pipe surrounding is ignored in the model. The pipeline roughness was found
264 experimentally to be 0.005 mm, while the ambient pressure was 1.01 bara.

265 ### 3.3.1. Binary mixture

266 Figure 7 shows comparison of the predicted and measured variation of the pressure at the closed
267 end of the section of pipeline following the initiation of the decompression. As may be observed in
268 the predicted results, the pressure remains initially constant but falls rapidly at ca. 0.2 s when the
269 initial expansion wave, caused by the decompression, reaches the closed end of the pipeline. The
270 experimental pressures shown were sampled with too low frequency to resolve this. Following this,
271 a pressure plateau of ca. 58 bara is predicted, until ca. 2.5 s at which point the pressure begins to fall
272 again towards the ambient. In comparison, after the initial pressure drop, the experimental pressure
273 is observed to fall more slowly to a minimum at ca. 1 s before recovering to a pressure very close to
274 the plateau pressure predicted by the model. This is practically important as this pressure is that
275 which is used in the analysis of the propagation of ductile fractures (Mahgerefteh et al., 2012a).
276 Following this the pressure again drops, but at a slower rate than that predicted. As noted by various
277 authors (Mahgerefteh et al., 2012b; Munkejord et al., 2010) this later behaviour is largely due to
278 frictional and heat transfer effects, the modelling of which is outside of this study.

279 Figure 8 shows the thermodynamic trajectory at the closed end of the pipeline section during the
280 decompression relative to the dew and bubble lines. As may be observed, as noted above, during
281 the initial decompression the fluid drops almost instantaneously along the isentrope into the phase
282 envelope where it descends towards the dew line at low temperatures.

283 ### 3.3.2. Quinternary mixture

284 Figure 9 shows the comparison of the predicted pressures with the experimental data recorded at
285 transducers P14 and P18 , 1.84 m and 3.64 m from the open end of the pipeline respectively
286 (Cosham et al., 2012). As may be observed, at both P14 and P18 the time at which the initial
287 pressure drop occurs, 2.75 and 5.5 ms respectively, is well captured. The recorded pressure during
288 the initial decompression is seen to be slower than that predicted; this deviation can partially be
289 explained by a lag in the measurements, given the rapidity in the pressure change.

290 Following this initial period of transients the simulations predict a steadying of the pressure at ca. 65
291 bara, at P18 this lasts for the duration of the simulation while for P14 the pressure begins to fall at
292 ca. 36 ms. In contrast, the measured data fall steadily throughout this period, this is likely in part due
293 to the effects of friction and heat transfer which the fluid model applied here does not capture
294 accurately (Mahgerefteh et al., 2012b). Notably the measured pressure at P14 indicates a
295 subsequent acceleration of the pressure drop at the time predicted by the fluid model.

4. Conclusions

This paper presents the development and application of a robust interpolation technique for the prediction of thermodynamic properties and phase equilibria of complex mixtures. The accuracy and computational burden of computing these physical properties greatly affects the overall accuracy and computational cost of multiphase multicomponent simulations. Thus, the adaption of this technique has a tremendous impact on our ability to perform sophisticated computational fluids dynamics (CFD) simulations at reasonable cost without significant loss of accuracy.

The assessment of the technique's ability to reproduce the results of the EoS showed, for the most part, an error no greater than 0.5 % compared to the actual EoS predictions. Large errors were observed only for the liquid phase at low temperatures, where the physical model represented by the EoS is itself not applicable, as solid formation not predicted by the EoS is expected. The extension of the current interpolation technique to a thermophysical model where the solid phase is accounted for is part of ongoing work.

Following this, the method was coupled with a fluid model and was used for the simulation of CO_2 rich mixtures, which is of particular interest in the development of CCS technology. Analysis of several hypothetical shock tube tests, as well as the comparison of the predictions against experimental decompression data, showed that the interpolation method produced robust and highly reliable results for simple and complex mixtures.

Interestingly, comparison between model predictions and experimental decompression results showed that the implementation of the interpolation technique produced a reasonable prediction of the initial depressurisation period. On-going work by the authors focuses on the development of appropriate models for the heat transfer and frictional effects to improve the accuracy of the predictions beyond this period.

5. Acknowledgements

6. References

Akima, H., 1996. Algorithm 761: Scattered-data surface fitting that has the accuracy of a cubic polynomial. ACM Trans. Math. Softw. 22, 365–371.

Andresen, T., 2009. Mathematical modeling of CO2 based heat pumping systems. PhD Thesis. NTNU.

Blinkov, V., Jones, O., Nigmatulin, B., 1993. Nucleation and flashing in nozzles—2. Comparison with experiments using a five-equation model for vapor void development. Int. J. Multiph. Flow 19, 965–986.

Brown, S., Fraga, E.S., Mahgerefteh, H., Martynov, S., 2015a. A geometrically based grid refinement technique for multiphase flows. Comput. Chem. Eng. 82, 25–33. doi:10.1016/j.compchemeng.2015.05.031

Brown, S., Martynov, S., Mahgerefteh, H., 2015b. Simulation of two-phase flow through ducts with discontinuous cross-section. Comput. Fluids 120, 46–56. doi:10.1016/j.compfluid.2015.07.018

Castier, M., 2009. Solution of the isochoric–isoenergetic flash problem by direct entropy

336   maximization. Fluid Phase Equilib. 276, 7–17. doi:10.1016/j.fluid.2008.10.005

337   Chen, N.H., 1979. An Explicit Equation for Friction Factor in Pipe. Ind. Eng. Chem. Fundam. 18, 296–
338   297. doi:10.1021/i160071a019

339   Cosham, A., Jones, D.G., Armstrong, K., Allason, D., Barnett, J., 2012. The Decompression Behaviour
340   of Carbon Dioxide in the Dense Phase, in: Proceedings of the 2012 9th International Pipeline
341   Conference. Asme, p. 447. doi:10.1115/IPC2012-90461

342   Diamantonis, N.I., Boulougouris, G.C., Mansoor, E., Tsangaris, D.M., Economou, I.G., 2013a.
343   Evaluation of Cubic, SAFT, and PC-SAFT Equations of State for the Vapor–Liquid Equilibrium
344   Modeling of CO2 Mixtures with Other Gases. Ind. Eng. Chem. Res. 52, 3933–3942.
345   doi:10.1021/ie303248q

346   Diamantonis, N.I., Boulougouris, G.C., Tsangaris, D.M., Kadi, M.J. El, Saadawi, H., Negahban, S.,
347   Economou, I.G., 2013b. Thermodynamic and transport property models for carbon capture and
348   sequestration (CCS) processes with emphasis on CO2 transport. Chem. Eng. Res. Des. 91, 1793–
349   1806. doi:10.1016/j.cherd.2013.06.017

350   Diamantonis, N.I., Economou, I.G., 2011. Evaluation of Statistical Associating Fluid Theory (SAFT) and
351   Perturbed Chain-SAFT Equations of State for the Calculation of Thermodynamic Derivative
352   Properties of Fluids Related to Carbon Capture and Sequestration. Energy & Fuels 25, 3334–
353   3343. doi:10.1021/ef200387p

354   Dumbser, M., Iben, U., Munz, C.D., 2013. Efficient implementation of high order unstructured WENO
355   schemes for cavitating flows. Comput. Fluids 86, 141–168.
356   doi:10.1016/j.compfluid.2013.07.011

357   Kontogeorgis, G.M., Folas, G.K., 2010. Thermodynamic Models for Industrial Applications: From
358   Classical and Advanced Mixing Rules to Association Theories. Wiley.

359   Leveque, R.J., 2002. Finite Volume Methods for Hyperbolic Problems. Cambridge University Press,
360   Cambridge.

361   Liou, M., 2006. A sequel to AUSM, Part II: AUSM+-up for all speeds. J. Comput. Phys. 214, 137–170.
362   doi:10.1016/j.jcp.2005.09.020

363   Mahgerefteh, H., Brown, S., Denton, G., 2012a. Modelling the impact of stream impurities on ductile
364   fractures in CO2 pipelines. Chem. Eng. Sci. 74, 200–210. doi:10.1016/j.ces.2012.02.037

365   Mahgerefteh, H., Brown, S., Martynov, S., 2012b. A study of the effects of friction, heat transfer, and
366   stream impurities on the decompression behavior in CO2 pipelines. … Gases Sci. … 379, 369–
367   379. doi:10.1002/ghg

368   Mahgerefteh, H., Oke, a, Rykov, Y., 2006. Efficient numerical solution for highly transient flows.
369   Chem. Eng. Sci. 61, 5049–5056. doi:10.1016/j.ces.2006.03.012

370   Martynov, S.B., Mason, D.J., Heikal, M.R., 2006. Numerical Simulation of Cavitation Flows Based on
371   Their Hydrodynamic Similarity. Int. J. Engine Res. 7, 283–296. doi:10.1243/14680874JER04105

372   Michelsen, M., 1982. The isothermal flash problem. Part II. Phase-split calculation. Fluid Phase
373   Equilib. 9, 21–40. doi:10.1016/0378-3812(82)85002-4

374   Michelsen, M.L., 1999. State function based flash specifications. Fluid Phase Equilib. 158-160, 617–
375   626. doi:10.1016/S0378-3812(99)00092-8

376   Michelsen, M.L., 1982. The isothermal flash problem. Part I. Stability. Fluid Phase Equilib. 9, 1–19.

377   Munkejord, S.T., Hammer, M., 2015. Depressurization of CO2-rich mixtures in pipes: Two-phase flow

378   modelling and comparison with experiments. Int. J. Greenh. Gas Control 37, 398–411.
379   doi:10.1016/j.ijggc.2015.03.029

380   Munkejord, S.T., Jakobsen, J.P., Austegard, A., Mølnvik, M.J., 2010. Thermo- and fluid-dynamical
381   modelling of two-phase multi-component carbon dioxide mixtures. Int. J. Greenh. Gas Control
382   4, 589–596. doi:10.1016/j.ijggc.2010.02.003

383   Porter, R.T.J., Fairweather, M., Pourkashanian, M., Woolley, R.M., 2015. The range and level of
384   impurities in CO2 streams from different carbon capture sources. Int. J. Greenh. Gas Control 36,
385   161–174. doi:10.1016/j.ijggc.2015.02.016

386   Saha, S., Carroll, J.J., 1997. The isoenergetic-isochoric flash. Fluid Phase Equilib. 138, 23–41.
387   doi:10.1016/S0378-3812(97)00151-9

388   Simões-Moreira, J.., Bullard, C.., 2003. Pressure drop and flashing mechanisms in refrigerant
389   expansion devices. Int. J. Refrig. 26, 840–848. doi:10.1016/S0140-7007(03)00070-7

390   Span, R., Wagner, W., 1996. A New Equation of State for Carbon Dioxide Covering the Fluid Region
391   from the Triple-Point Temperature to 1100 K at Pressures up to 800 MPa. J. Phys. Chem. Ref.
392   Data 25.

393   Zucrow, M.J., Hoffman, J.D., 1975. Gas Dynamics. Wiley, New York.

394

395

396

397 **Table 1. Initial conditions and fluid composition for decompression experiments Test 26 and 31**
398 **(Cosham et al., 2012).**

Input Parameter	Test 26	Test 31
Feed Inlet Temperature (K)	278.35	283.15
Feed Inlet Pressure (bar)	141	151.51
Fluid Composition (% vol./vol)	N_2 : 4.04 CO_2 : 95.96	H_2 : 1.15 N_2 : 4.0 O_2 : 1.87 CH_4: 1.95 CO_2 : 91.03

399

400 **Table 2. Average absolute deviations (%) of predictions of the temperature and pressure produced**
401 **by the interpolation grids.**

Input Parameter	Binary	Quinternary
Temperature	0.005	0.002
Pressure	0.44	0.07

402

403

404 **Table 3. Initial states for the single-phase shock tube tests**

Input Parameter	P (bara)	Temperature (K)	Velocity (m s^{-1})
Left state	151	283.15	0
Right state	100	260.00	0

405

406 **Table 4. Initial states for the two-phase shock tube tests**

Input Parameter	P (bara)	Temperature (K)	Velocity (m s^{-1})
Left state	151	283.15	0
Right state	P_{dew}+2	260.00	0

407

408

(a)   (b)
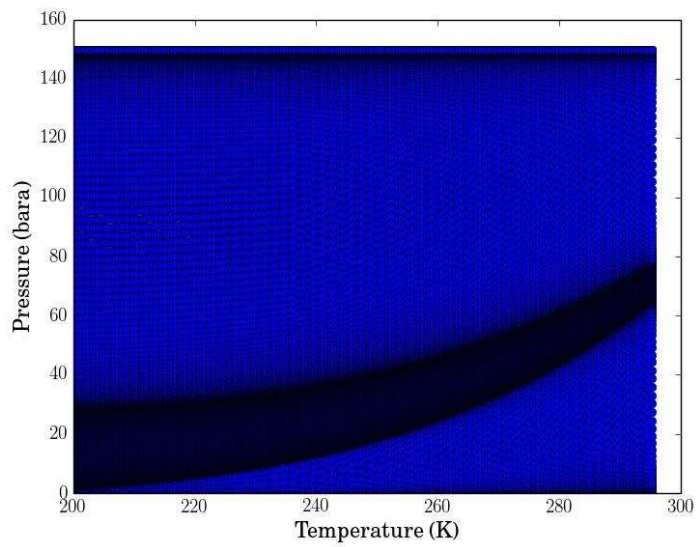
409
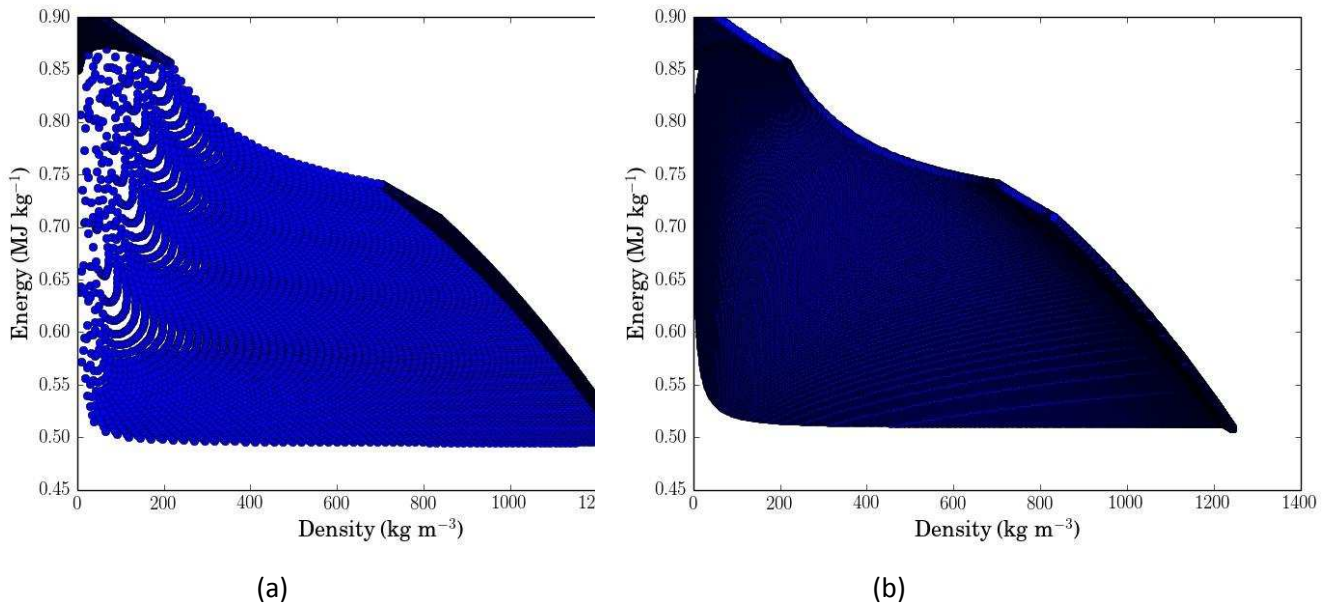
Figure 1: The $\{\rho, e\}$ interpolation grids in the case of a uniform sampling (a) and with the adaptive sampling method (b) produced for the binary mixture of 95.96 % CO_2 - 4.04 % N_2 (vol/vol).
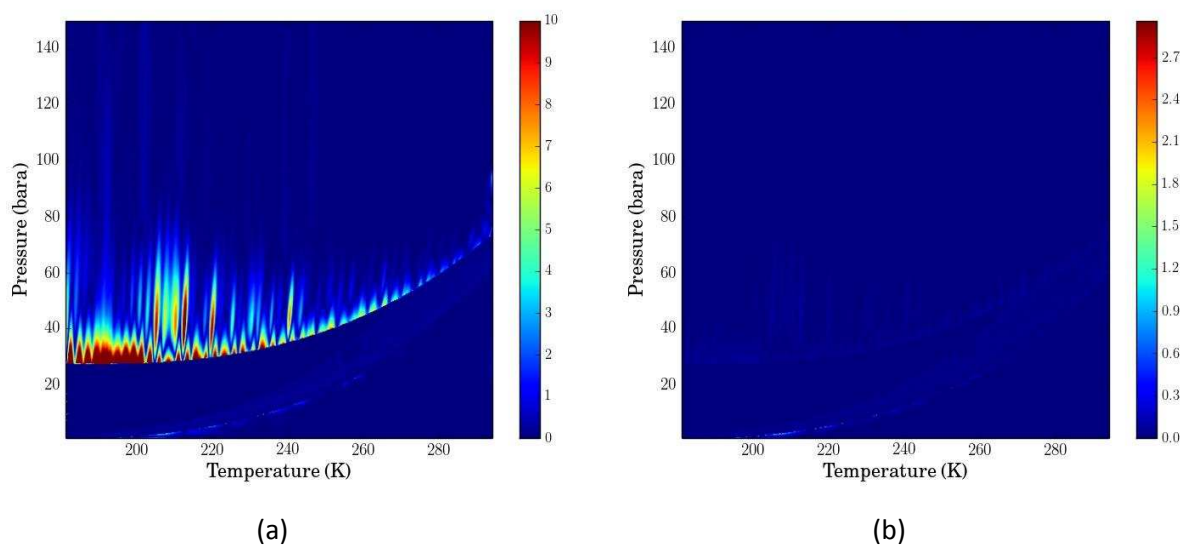
412

413

Figure 2: The {P,T} interpolation grid produced with the adaptive sampling method for the binary mixture of 95.96 %CO_2 - 4.04 % N_2 (vol/vol).
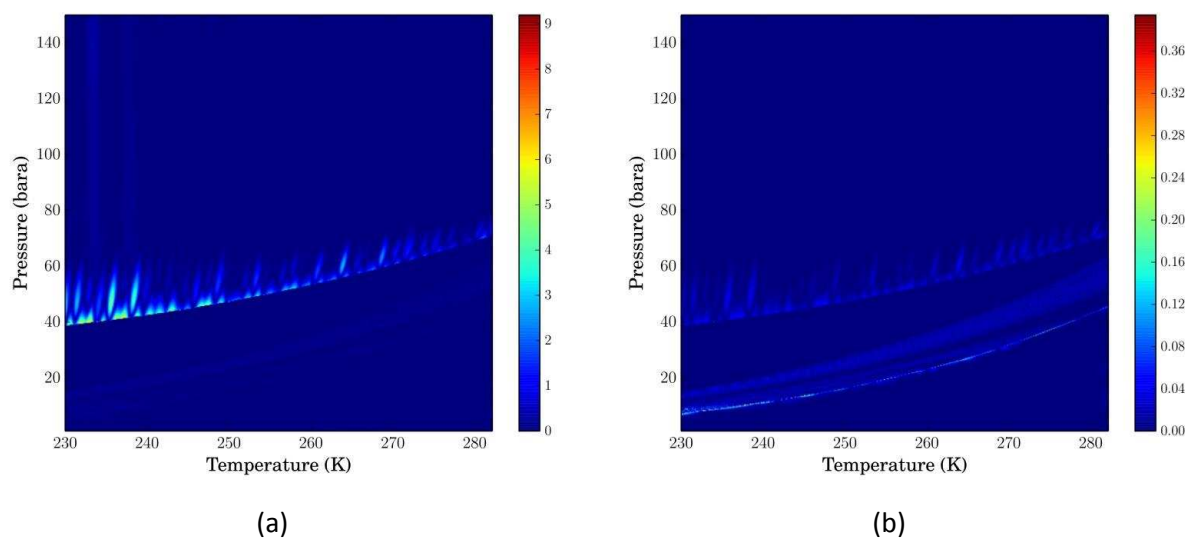
416

417

418

419

(a)   (b)

420

Figure 3: %AAD interpolation errors observed in the pressure (a) and temperature (b) across the relevant region in the P-T phase diagram for the binary mixture.

423

424

425

(a)   (b)

426

Figure 4: %AAD interpolation errors observed in the pressure (a) and temperature (b) across the relevant region in the P-T phase diagram for the quinternary mixture.

429

430

431

432
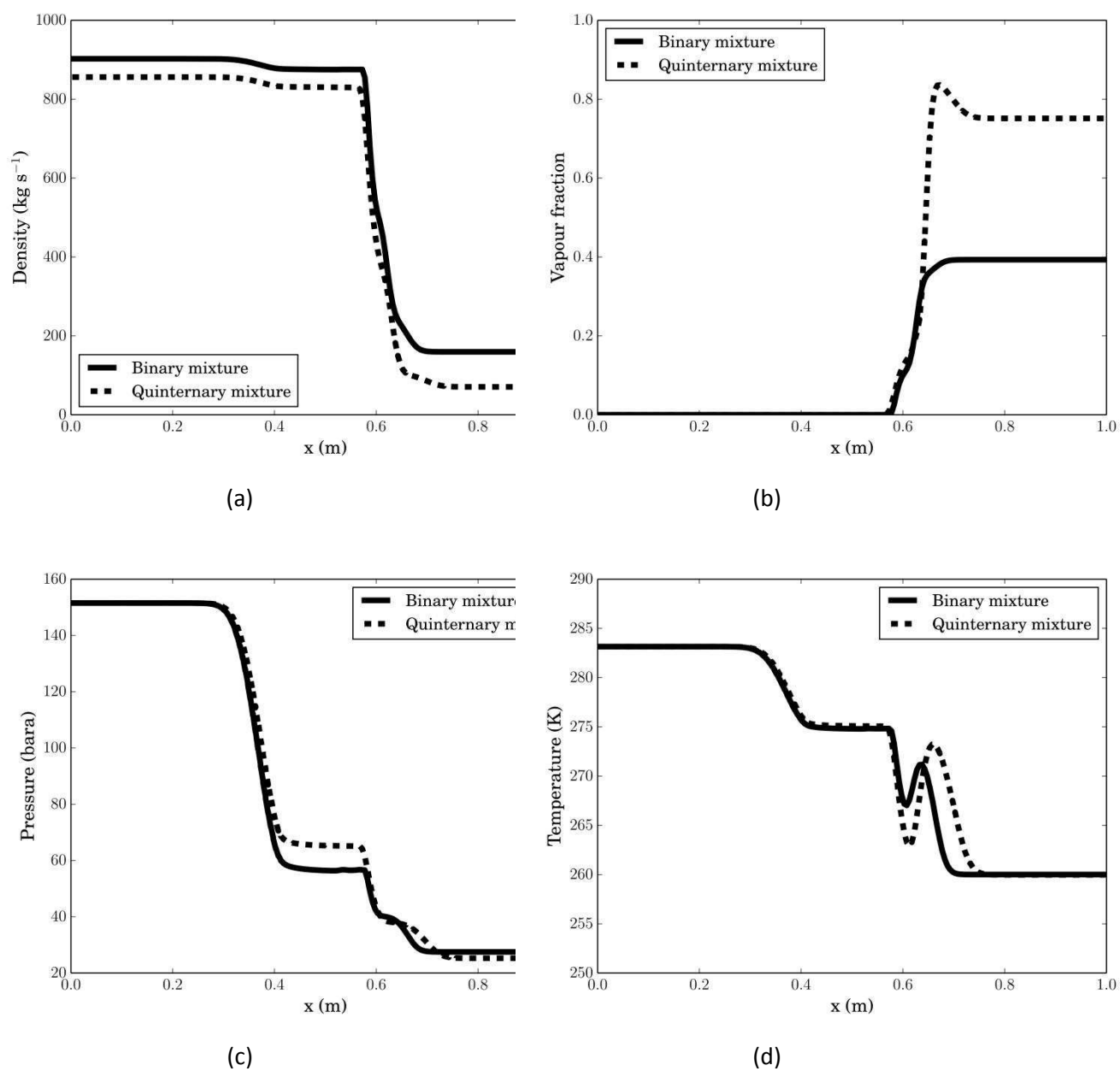

(a)   (b)

(c)
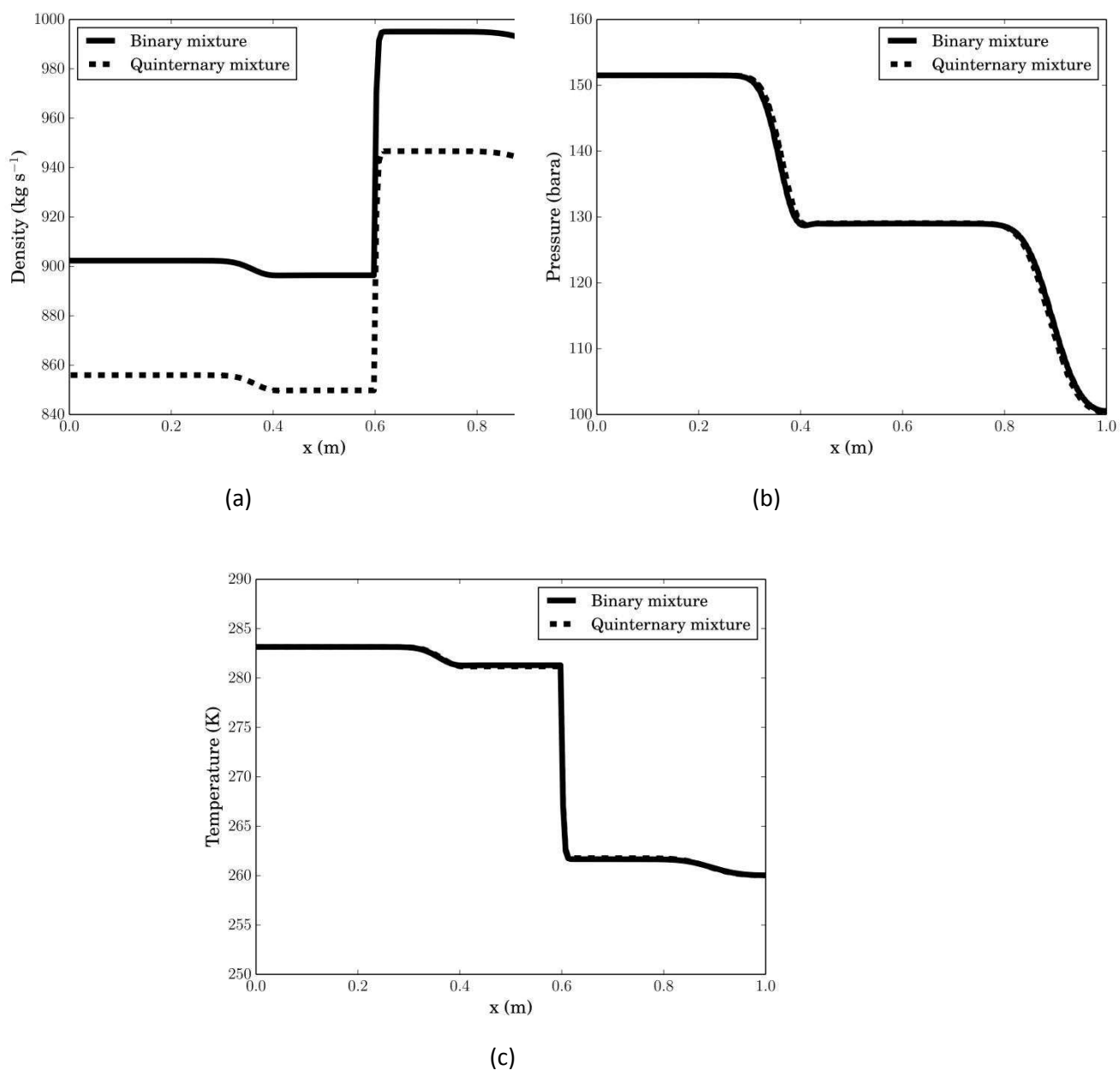
**Figure 5: Comparison of binary and quinternary mixture profiles of density (a), pressure (b) and
temperature (c) for the single-phase shock tube test after 0.4 ms.**

435

436

437
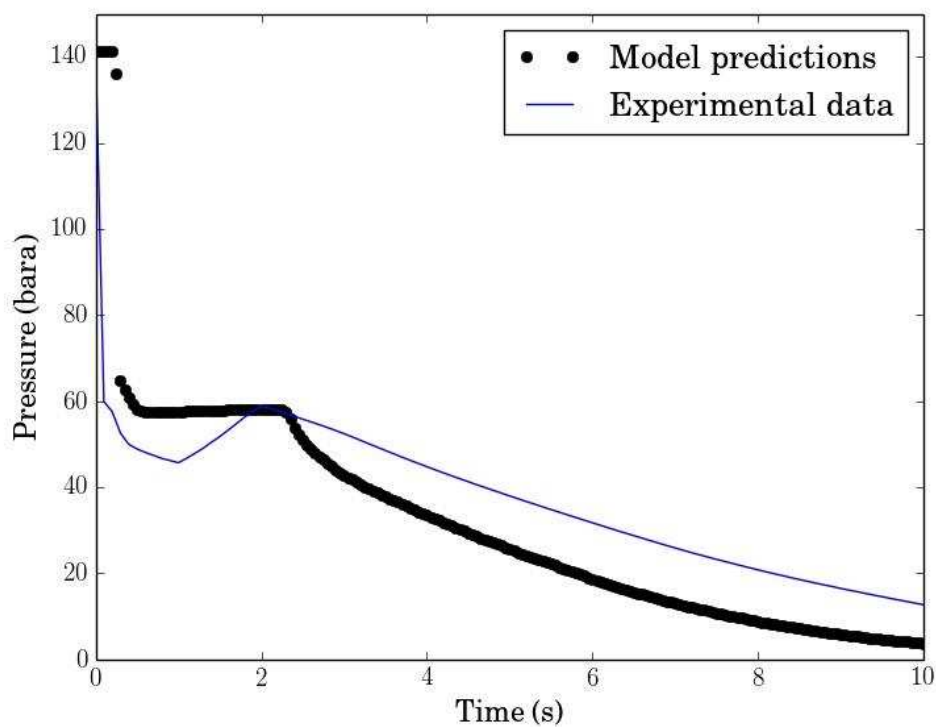

(a)   (b)

(c)   (d)
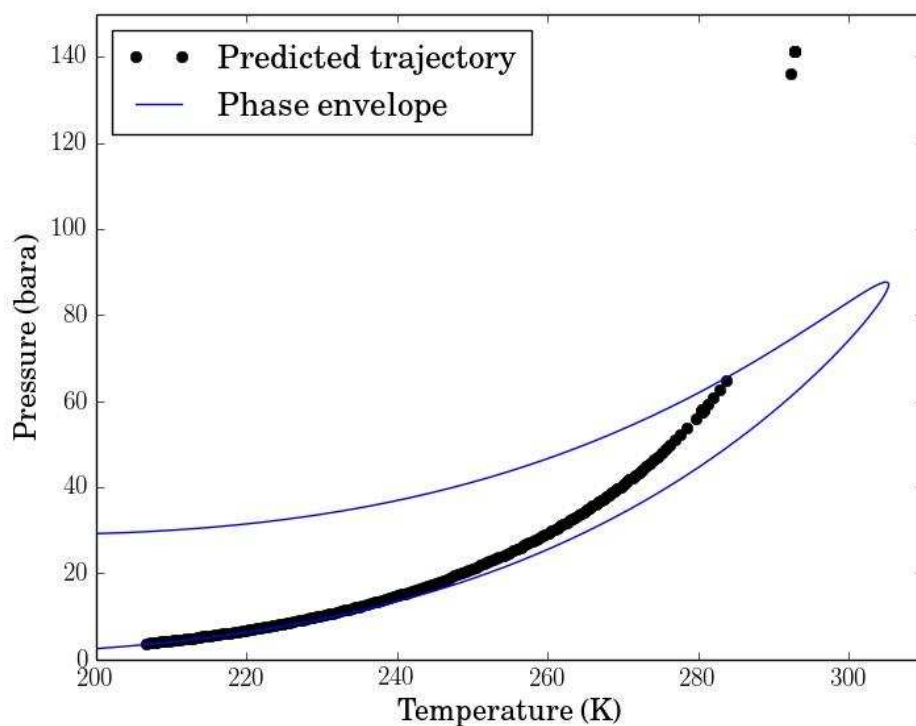
438

**Figure 6: Comparison of binary and quinternary mixture profiles of density (a), vapour fraction (b),
pressure (c) and temperature (d) for the two-phase shock tube test after 0.4 ms.**

441

442

443 **Figure 7: Comparison of the predicted and measured variation of pressure with time at the closed**
444 **end of the pipeline following the initiation of decompression.**

445

446 **Figure 8: Thermodynamic trajectory of the decompression relative to the binary mixture phase**
447 **envelope at the closed end of the pipeline following the initiation of decompression.**
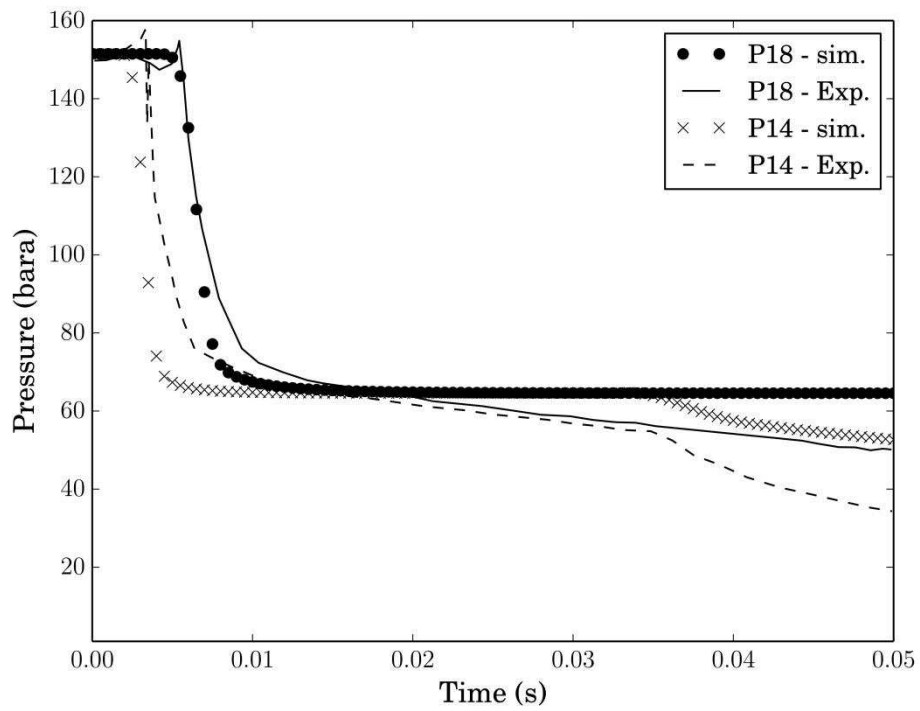
448

449 **Figure 9: Comparison of the predicted and measured variation of pressure with time 1.84 m (P14)**
450 **and 3.84 (P18) from the open end of the pipeline following the initiation of decompression for the**
451 **case of quinternary mixture.**

452